Available online at www.sciencedirect.com

ScienceDirect

Advances in Space Research xx (2022) xxx-xxx

ADVANCES IN SPACE RESEARCH (a COSPAR publication)

www.elsevier.com/locate/asr

Forecasting of cosmic rays intensities with HelMod Model

M. J. Boschini[a,b], S. Della Torre[a,*], M. Gervasi[a,c], G. La Vacca[a,c], P. G. Rancoita[a]

[a] *INFN sez. Milano-Bicocca, Piazza della Scienza, 3 - 20126 Milano (Italy)*
[b] *also CINECA, Segrate, Milano, Italy*
[c] *also Physics Department, University of Milano-Bicocca, Piazza della Scienza, 3 - 20126 Milano (Italy)*

Abstract

HelMod model allows one to describe how solar modulation affects the propagation of galactic cosmic rays (GCR) through the heliosphere with an accuracy of the level of actual experimental uncertainties. The GCRs mainly constitute the high energy population of the so-called space radiation environment. The model treats the physical processes involved in solar modulation, like diffusion, particle drift, convection and adiabatic energy losses, and it embeds a description of both the inner and outer heliosphere. To obtain the modulated intensities, the model requires the knowledge of a few time-dependent heliospheric quantities, i.e., sunspot number, tilt angle of the neutral current sheet, solar wind speed and density, and interplanetary magnetic field. Using historical records, we present a template-based procedure that allows one to predict the heliospheric parameters for coming years, and, in turn, the forecasted modulated spectra. The *forecasting templates* reconstruct the typical time variation along with solar cycles and may be tuned to the current solar cycle. We estimate that the uncertainty of the forecasted cosmic rays intensity is below 5% (±10% at 68% C.L.) on average for short time predictions (up to 4 years), and below 15% (±(20 − 25)% at 68% C.L.) for long time predictions (up to 11 years).

Keywords: solar modulation; interplanetary space; Cosmic rays; space weather; sunspot number; space radiation environment; Forecast

1. Introduction

The interplanetary space is permeated by charged galactic cosmic rays (GCR) accelerated into the interstellar medium by, e.g., the explosions of supernovae (Baade & Zwicky, 1934; Koyama et al., 1995). The energy of a GCR particle is high enough to allow it to easily penetrate the thin shielding of most spacecraft. Thus, GCRs represent a potential radiation hazard for both electronic and biological materials in space (see, e.g., Durante & Cucinotta, 2008; Samwel & Hady, 2009; Gonzalez-Velo et al., 2017) and it is believed to be one of the major causes of spacecraft failures (Samwel et al., 2019). At Earth orbit, i.e., inside the region influenced by Sun-related processes, the GCR intensity shows a time variation related to solar activity (see, e.g., Potgieter, 2013, and reference therein). Samwel et al. (2019) demonstrated that *Single Event Effect* (SEE) on electronics in space has a larger occurrence during maximum solar activity than during minimum solar activity. Although, in general, the use of shielding material of at least 1.5mm of Al can reduce the radiation effects to acceptable levels, for both maximum and minimum solar activity for missions of moderate (∼3 years) duration (Samwel et al., 2019), the knowledge of space radiation environment is required to make a proper estimation of expected radiation damage experienced by satellites both at Earth and deep space orbits (ECSS, 2008).

The model describing particle propagation in the heliosphere was originally developed by Parker (1965): when GCRs encounter the heliosphere, they undergo additional propagation processes due to the interaction with the expanding solar wind and the solar magnetic field embedded in (Parker, 1965; Glee-

*Corresponding author
Email addresses: m.boschini@cineca.it (M. J. Boschini), stefano.dellatorre@mib.infn.it (S. Della Torre), massimo.gervasi@unimib.it (M. Gervasi), giuseppe.lavacca@unimib.it (G. La Vacca), piergiorgio.rancoita@mib.infn.it (P. G. Rancoita)

https://dx.doi.org/10.1016/j.jasr.xxxx.xx.xxx
0273-1177/

son & Axford, 1967; Jokipii & Parker, 1970; Jokipii, 1971; Fisk, 1971; Jokipii et al., 1977). The result is a global reduction of the differential intensity that is time and rigidity dependent. This is known as *solar modulation* as it appears as an inverse relationship between GCR intensities and solar activity through its well known 22-years cycle. A combination of new-generation space detectors (Martucci et al., 2018; Aguilar et al., 2018) and deep-space probes exploring the heliosphere (see, e.g., Simpson et al., 1992; Simpson, 1996; Heber et al., 1997; Stone et al., 2005; Webber & McDonald, 2013; Stone et al., 2013, 2019) shed a new light on this field (Fiandrini et al., 2021), leading to the development of more accurate models for the space radiation environment.

In this work, we present the forecasting tool of the HelMod[1] model (summarized in Sect. 2) which is currently capable to reproduce the observed modulated spectra since solar cycle 22 (Bobik et al., 2012; Della Torre et al., 2012; Boschini et al., 2017b, 2018b,c,a, 2019, 2020a,b, 2021a,b) with and accuracy of the level of actual experimental uncertainties (i.e. few percent for AMS-02 integrated spectra). In Sect. 3 we present the details of our template approach for forecasting *heliospheric parameters* using historical values. Finally, the accuracy of this method on forecasting GCR fluence was discussed in Sect. 4 with particular attention to assessing the use of the numerical model to evaluate the space radiation environment for missions of moderate (~3 years) duration.

2. The HelMod model: Heliospheric Propagation of Cosmic Rays

HelMod is a Monte Carlo code that solves the particle transport equation through the heliosphere (Boschini et al., 2018a, 2019, and reference there in). The model, based on the Parker Equation (Parker, 1965), describes the cosmic ray fluence measured at Earth orbit as a complex combination of diffusion on magnetic irregularities, adiabatic energy losses/gains due to the propagation in the expanding magnetic fields, effective convection resulting from the solar wind convection, and magnetic drift effects due to large scale magnetic structures in the heliosphere. These effects are related to the level of solar activity intensity, the solar magnetic field polarity, and are energy- and charge-sign-dependent. HelMod numerically solves a set of stochastic differential equations that are mathematically equivalent to Parker Equation. The code applies a Monte Carlo backwards-in-time approach as described in Bobik et al. (2016). The result of the simulation is a transformation matrix that once applied to the GCR spectra outside the heliosphere (Local Interstellar Spectra – LIS) produces the *modulated spectra*. LISs were derived through an iterative procedure in the so-called GALPROP-HelMod framework (Boschini et al., 2017b) that allowed to derive the LISs for particles with the atomic number $Z \leq 28$ from AMS-02 (Aguilar et al., 2021) and Voyagers (Cummings et al., 2016) observations (Boschini et al., 2017b, 2018b,c, 2020a,b, 2021b). Nowadays, the model is capable to reproduce the observed modulated spectra since solar cycle 22 (Bobik et al., 2012; Della Torre et al., 2012; Boschini et al., 2017b, 2018b,c,a, 2019, 2020a,b, 2021a,b). The HelMod accuracy is typically at the level of experimental uncertainties and it varies with time reflecting the uncertainties related to time-dependent and local heliospheric effects. For protons, the model accuracy may be guessed by inspecting, for instance, Figures 7 and 8 in Boschini et al. (2019) where the HelMod version 4 modulated spectra were compared with the modulated spectra observed by AMS-02 in the first three years of data taking and with observations from EPHIN, BESS, PAMELA and AMS-02 at 2GV. In the present model, the heliosphere is described as a sphere with a small compression in the so-called *nose* direction, defined by the relative motion of the Sun in the local bubble due to galactic rotation, and with a dimension that change with time as described in Boschini et al. (2019). The inner heliosphere[2] is then divided into 15 subregions, with different parameters, accounting for the time needed by the solar wind to propagate from the Sun. The model depends on several parameters that can be directly observed through *in-situ* or solar observations, the remaining free parameters were tuned using proton cosmic rays observations during the last two solar cycles as measured by particle detectors at Earth orbit and in deep space (Boschini et al., 2018a, 2019). The parameters inferred by observational measurements are related to the major heliospheric quantities, i.e., daily count and monthly smoothed sunspot number (SN), Tilt Angle of Neutral Current Sheet (TAL, Hoeksema, 1995), Solar Wind speed (SWS, in km/s), Solar Wind Proton Density (SWD, in N/cm^3), and Interplanetary magnetic field Magnitude (IMF, in nT). In Fig. 1 the heliospheric parameters used in HelMod are reported as a function of time. The daily value of SN, SWS, SWD, and IMF are extracted from NASA/GSFC's OMNI dataset (King & Papitashvili, 2005) through OMNIWeb[3]. The average values along Carrington Rotations of the TAL are extracted by Wilcox Solar Observatory[4]. Finally, the monthly smoothed sunspot number is extracted by the World Data Center SILSO, Royal Observatory of Belgium, Brussels[5]. From an inspection of Fig. 1 it is possible to note how many of these parameters show a cyclic behaviour with the same periodicity of the Solar Cycle. A closed look highlights the presence of regular structures even at short time scales that can be neglected, i.e., averaged, when considering studies for moderate duration missions.

3. Forecasting heliospheric parameters

The modulated GCR intensity is directly predicted employing the heliospheric parameters described in Sect. 2. Thus, the forecasting tool of the HelMod model is based on forecasting heliospheric parameters. The forecast algorithm proposed in

[1] Results presented in this article are also available through online calculators at http://www.helmod.org

[2] the space region bounded by the termination shock where the solar wind flows supersonically.

[3] https://omniweb.gsfc.nasa.gov/

[4] http://wso.stanford.edu/Tilts.html

[5] http://sidc.be/silso/home

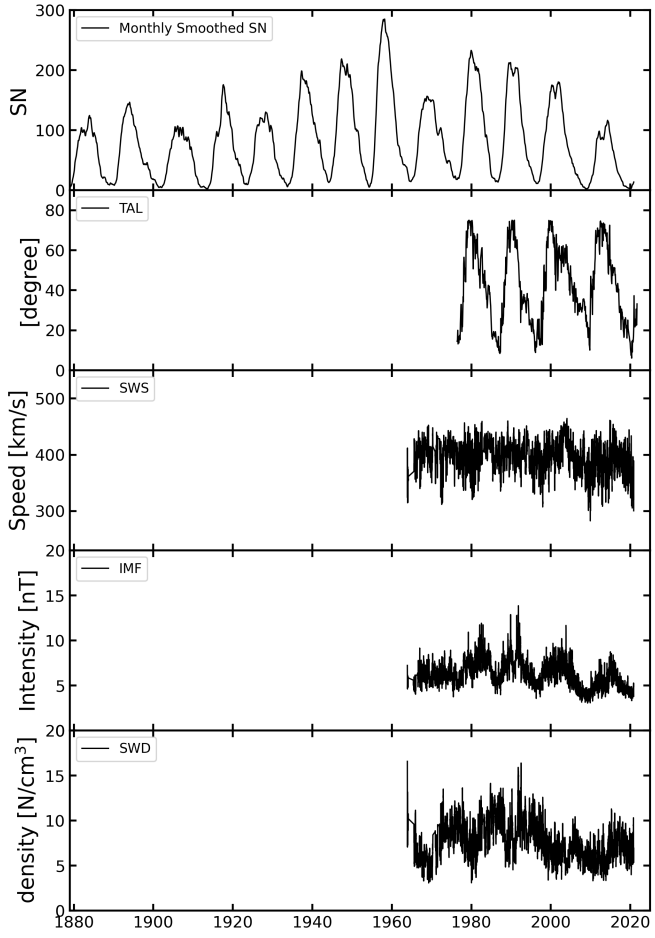

Fig. 1. The heliospheric parameters used by HELMOD and reported as a function of time.

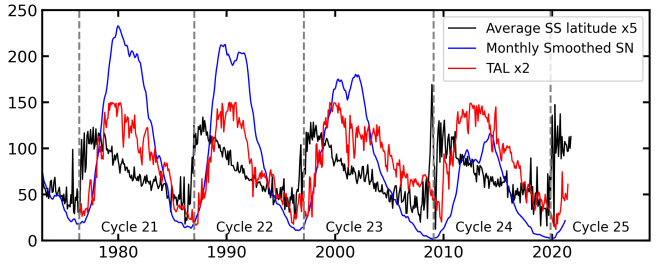

Fig. 2. Solar parameters over the last 4 Solar Cycles. The blue line shows the monthly smoothed SN, the black line is the average sunspot latitude scaled up by a factor of 5, the red line shows TAL values times a scaling factor of 2. Scaling factors are chosen to ensure a qualitative visual comparison. In general, the Solar Cycle variations of these parameters are quite similar, particularly during the rising phase, despite the marked difference in the magnitudes of monthly smoothed SN. We mark the start-time of a new cycle with vertical dashed lines.

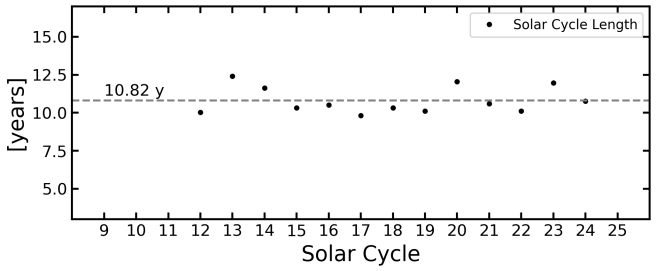

Fig. 3. Length of Solar Cycle according to Tab. 1. The dashed horizontal line represents the average solar cycle length.

this work was derived by the one described in Owens et al. (2011) (see also, Boschini et al., 2017a). In that article, the authors derived an *average solar activity* to estimate the most likely value of Sunspot Number, IMF and GCR intensity at the solar maximum as well the long-term solar variations. In addition, they compared their predicted values with those observed during Solar Cycle 24. In the present approach, the Owens et al. (2011) algorithm is revisited a) to include the data of Solar Cycle 24 and b) to study the secular-periodicity solar variation. The *Forecasting Template* for SN, IMF, SWS, TAL and SWD was evaluated using historical values since Solar Cycle 20 (Solar Cycle 11 for SN) combining values to provide a typical time evolution from one solar minimum to the next one. It has to be noted that, as stated in Owens et al. (2011), the choice to use the minimum value of SN to tag the start/end time of Solar Cycles leads to some ambiguity. For this reason, the average solar latitude of the sunspots (θ_s) can be better used to mark the beginning of the cycle. θ_s along with Monthly Smoothed SN and TAL values are shown in Fig. 2 since Solar Cycle 21. The latitudinal positions of Sunspots were extracted from the daily Solar Region Summary (SRS) compiled by SWPC[6] and from USAF/NOAA Sunspot Data database[7]. From an inspection of Fig. 2, one can note that, before the solar minima, sunspots mainly lie on the solar equator (i.e., the lowest value of θ_s). After solar minima, i.e., when TAL and SN start to increase, high latitude sunspot pairs appear, replacing equatorial sunspot pairs. Thus, the Solar Cycle starting-time can be defined as when θ_s sharply increases from ~10° to ~25° (Owens et al., 2011). The computed solar cycle starting epoch are reported in Fig. 2 and Tab. 1, while the length, in years, of each Solar Cycle, and the computed average value, are reported in Fig. 3. These are in agreement with those calculated by Owens et al. (2011) within 1-2 months.

To evaluate *Forecasting Templates*, historical values of SN, IMF, SWS, TAL and SWD were folded cycle by cycle. The time/phase of each cycle was set to the initial value of 0 and the final value of π. As one can note from Fig. 1, each solar cycle presents different maximum (and minimum) values, to allow for a comparison among the solar cycles, to focus the atten-

[6]The SRS contains a detailed description of the active regions visible, for the specific day, on the solar disk. All SRS reports of the active solar regions observed during the preceding day, beginning in 1996, are online in the SWPC Warehouse at ftp://ftp.swpc.noaa.gov/pub/warehouse .

[7]The sunspot database inherit the Royal Greenwich Observatory observations from 1874 to 1976, and extend them up to 2016. The database is available as ascii files at https://solarscience.msfc.nasa.gov/greenwch.shtml .

Table 1. The epoch of starting-time of Solar Cycles 12–25. Starting-time is defined using the sharp increase in average sunspot latitude (see the text). The table reports also the Scaling factors to yield the average value of SN, IMF, SWS, and SWD template to reproduce the solar cycle conditions (see the text).

		Scaling Factors			
Cycle	Start Year	SN	SWS	IMF	SWD
12	1879.22	0.70	–	–	–
13	1889.25	0.78	–	–	–
14	1901.66	0.64	–	–	–
15	1913.30	0.86	–	–	–
16	1923.61	0.78	–	–	–
17	1934.13	1.15	–	–	–
18	1943.95	1.27	–	–	–
19	1954.27	1.62	–	–	–
20	1964.38	0.95	–	1.01	0.96
21	1976.42	1.36	1.00	0.99	1.15
22	1987.02	1.25	0.93	1.01	1.19
23	1997.12	1.01	1.03	0.99	0.89
24	2009.09	0.61	1.02	0.98	0.86
25	2019.86	–	–	–	–

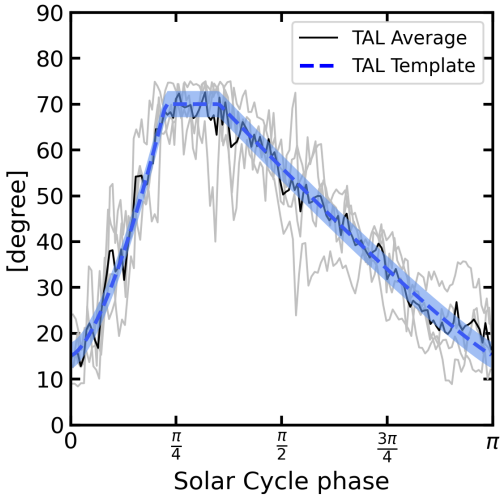

Fig. 4. TAL rescaled to set the initial value to 0 and final value to π (grey lines). The blue-dashed, TAL template, is the analytical interpolation of the mean value for each solar cycle phase, while the blue-shaded area represents its standard deviation.

tion on the relative variations from minimum to maximum (and vice-versa), we evaluate the heliospheric quantity mean values for each solar cycle and use this value as normalization factor: all heliospheric quantities, except TAL, were scaled to have the same mean value. Hereafter the numerical factors used for such kind of normalization are referred to as *scaling factors*. By construction, TAL cannot exceed $\sim 75°$ that is reached during solar maxima, therefore, it does not need a scaling procedure that equalizes all cycles for the comparison. The applied scaling procedure allows us to visualize how each solar parameter evolves along the solar cycle as reported in Figs. 4 and 5-left. It is also evident how all solar cycles show similar behaviour. In Fig. 4, we show TAL evolution along the solar cycle for the several analyzed cycles, together with its average value (black continuous line) and the analytical interpolation (blue dashed line). Such an analytical interpolation is then defined as the smooth *Forecasting Template*. To assess the uncertainties of *Forecasting Templates* (blue-shaded area in Fig. 4) we consider the standard deviation of residual between analytical interpolation and average value (in case of SN we directly evaluate the standard deviation from historical values).

SWS, SN, IMF, and SWD *Forecasting Templates* were reported in Fig. 5-left. By construction, the SN template has a smooth shape along the cycle, thus can be directly used for forecast purposes, without the need for analytical interpolation. SWS, IMF and SWD templates, on the other hand, presents fine structures that are due to short- to medium-term transients that can be ignored for the purpose of long-term forecasting, hence the fit to smooth them out. Therefore, they are fitted (blue-dashed line) using a cyclic shape which is defined solely by the cycle phase (x) and can be described by the general form:

$$T(x) = q_0 \sin(q_1 x + q_2)^{q_3} + q_4 \quad (1)$$

with parameters q_i reported in Tab. 2. For TAL we used the analytical expression proposed by Cliver & Ling (2001); Alanko-Huotari et al. (2006):

$$TAL(x) = s(N) \cdot \begin{cases} p_0 + g\left(\frac{x}{\pi}\right)^{p_2} & , \text{if } x <= p_4\pi \\ f & , \text{if } p_4 \leq \frac{x}{\pi} \leq p_5 \\ p_0 + p_1\left[1 - \left(\frac{x}{\pi}\right)\right]^{p_3} & , \text{if } x > p_5\pi \end{cases} \quad (2)$$

where $p_4 < p_5$, $f = p_0 + p_1(1 - p_5)^{p_3}$, and $g = \frac{f - p_0}{p_4^{p_2}}$ to ensure continuity of the function. Parameters p_i are reported in Tab. 2.

The template *scaling factors* are then computed again to reproduce amplitudes in each solar cycle as reported in Tab. 1 and, with red points, in Fig. 5-right. Due to the availability of long term historical parameters on SN, one can note in Fig. 5-right the presence of a secular cycle that is now facing its minimum following the behaviour of the so-called *Gleissberg cycle* (see, e.g., Hathaway, 2015; Usoskin, 2017). It should be noted that this assumption limited the forecasting to near-future only, this because it's known that the periodical variation fails to reproduce the past Dalton and Maunder minima, so it's reasonable to expect similar failures in future solar cycles. From Fig. 5 it is also evident that cycle 20 cannot be described by the smooth secular variation. This is probably due to peculiar phenomena that should be treated separately and do not represent the general long time periodicity. This long-term variation in SN *scaling factor* was fitted with a sinusoidal curve in the form:

$$s(N) = a \sin(bN + c) + d \quad (3)$$

where N is the solar cycle number and a, b, c and d values are reported in Tab. 3.

SWS does not show any secular variation, thus we consider a mean value as a reference for forecasting. IMF and SWD, otherwise, show a decreasing time variation that is loosely correlated with the trend observed for the same period in SN scaling

Table 2. Computed parameters for Eqs. (1) and (2) with the corresponding uncertainties.

	q_0	q_1	q_2	q_3	q_4	
SWS	18. ± 3.	1.	0.	1.	383. ± 2.	
IMF	2.2 ± 0.1	1.	0.	2.	5.17 ± 0.05	
SWD	1.01 ± 0.08	2.	7.70 ± 0.05	1.	-3.63 ± 0.08	
	p_0	p_1	p_2	p_3	p_4	p_5
TAL	17. ± 1.	87. ± 3.	2.5 ± 0.2	1.21 ± 0.07	0.201 ± 0.003	0.355 ± 0.001

Table 3. Secular variation parameters described in Eq. (3) with the corresponding uncertainties. Since SWS does not exhibit a secular variation, Eq. (3) reduces to a constant value $s(N) = d$

	a	b	c	d
SN	0.49 ± 0.06	0.55 ± 0.02	9.5 ± 0.04	1.04 ± 0.04
SWS	–	–	–	0.992 ± 0.008
IMF	0.20 ± 0.04	0.55	9.5	1.02 ± 0.03
SWD	0.28 ± 0.07	0.55	9.5	1.01 ± 0.04

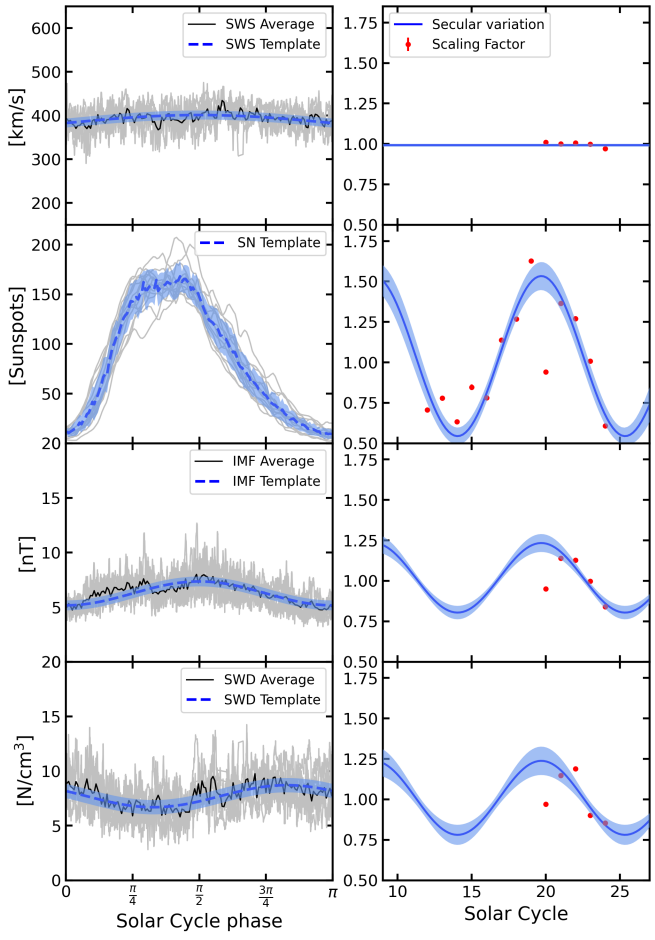

Fig. 5. Left: from top to bottom, VSW, SN, IMF, and SWD values were rescaled to set the initial value to 0 and final value to π and normalized to the same mean value (grey lines). The black solid line indicates the mean value for each solar cycle phase, while the blue-shaded area represents the standard deviation. The *forecasting template* is reported with a blue-dashed line. Right: Scaling factor for *forecasting templates* (red points) compared with secular variation (blue solid line) computed from Eq. (3), while the blue-shaded area represents 1-σ fit uncertainties; SWS does not exhibit any secular variation.

factor. Supposing a possible physical correlation between these parameters, it is reasonable to assume that also a secular variation of scaling factor should have the same period and phase. Thus, in Tab. 3 when evaluating Eq. (3) for IMF and SWD, we fixed period and phase parameters to be the same of SN solution while amplitude (a) and constant term (d) are obtained from the fit.

3.1. Forecasting procedure

Forecasting templates provide the typical shape of heliospheric parameter evolution through a solar cycle. Each template depends on two *forecasting parameters*: the length of the solar cycle and the scaling factor (except TAL that in this work depends on solar cycle length only). Here we describe the procedure to evaluate the *forecasting parameters* for each template using a data-driven approach fitting the fraction of the current solar cycle already available. The procedure to forecast a not-yet-started solar cycle is more complex and described later in the text. Even if we have a procedure to estimate the average cycle length and the secular scaling factor through different solar cycles, to get a more precise forecast we need to consider each solar cycle independently. This procedure can be applied from the actual date to the following solar minimum. We identify three cases based on the fraction of the current solar cycle already available:

a) *less than 3 years*. This boundary is the minimum rising phase length. The solar cycle is in its early stage and peculiar features are not yet evident. The template is evaluated using input from the average solar cycle length as well the scaling factor predicted from secular variation described by Eq. (3).

b) *Between 3 and 6 years*. The two boundaries are the minimum and the maximum length of the rising phase. During this period the solar cycle reaches its maximum and begins the descending phase. This implies that a fitting procedure on available data from the previous solar minimum can be performed, but the results must be compared with those

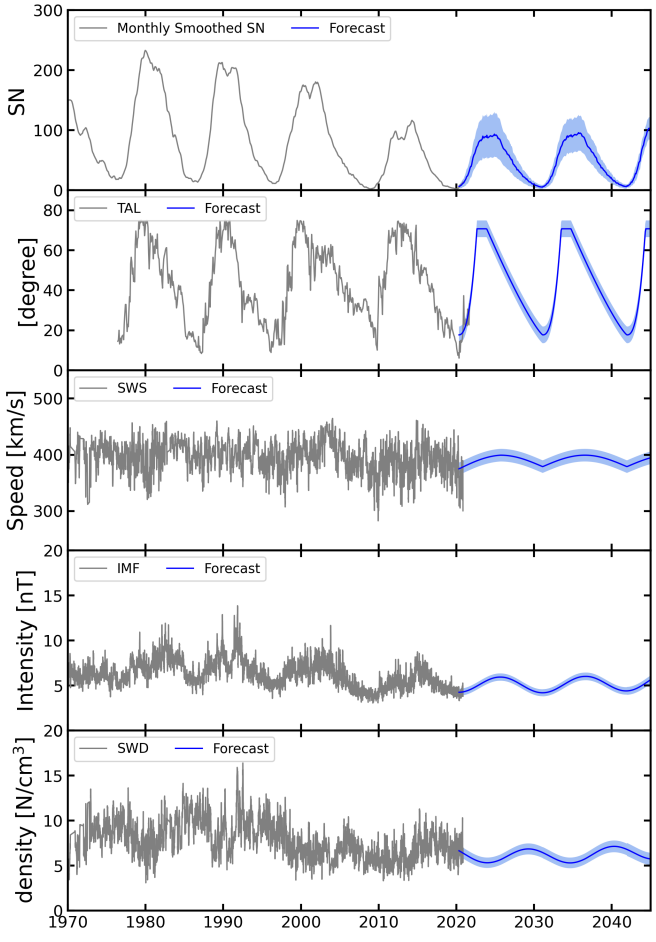

Fig. 6. Predicted heliospheric parameters for 25 years (blue solid line) together with the historical values from the last two solar cycles (grey line). The blue-shaded area is the sum in quadrature of *forecasting template* and secular variation uncertainties in Fig 5.

predicted by secular variation Eq. (3). We choose as acceptance criterion that the two values agree within 2.58σ that is equivalent to a confidence level of 99%. In case of criterion is not met, the procedure described in case (a) is applied.

c) *More than 6 years*. The solar cycle is facing the descending phase. Unless anomalous (unpredictable) features, like a shorter or longer duration of the cycle in comparison with the average, the overall shape of the solar cycle can be evaluated by fitting the available data with the *forecasting template*.

We evaluate solar cycle length and the scaling factor separately. To evaluate solar cycle length we used TAL and SN. The first template depends only on solar cycle length, while for SN cycle length and scaling factor should be fitted at the same time, but only the first parameter is considered at this stage. The solar cycle lengths obtained from the two fits are averaged using the error from the fit as weight and is assumed as a fixed parameter while evaluating the scaling factor for SWS, IMF, and SWD.

On the other hand, as described above, parameters of a new solar cycle, following the minimum at the end of the current cycle, can be inferred using only the average solar cycle length as well the scaling factor predicted from secular variation described by Eq. (3). To guarantee the continuity in the forecasted values, we introduced a transition function that ensures that, at solar maxima, the scaling factor is the one obtained from the procedure described above, while at solar minima *forecasting parameters* assume a value in between the ones of the two cycles[8].

Using available data, the length of solar cycle 25 is estimated to be 10.9 ± 0.8 years long with the next solar minima expected around the year 2031 ± 1. The Solar maximum should be reached in 2023 with a level of solar activity comparable (or a bit lower) with that observed in solar cycle 24. The same level may be reached in solar cycle 26 starting a new era of increasing solar activity in subsequent solar cycles. This estimation is in agreement with the physics-based solar cycle predictions for sunspot cycle 25 presented in Nandy (2021) that forecast a weak to a moderately weak cycle that will peak around 2024 (± 1). Predicted heliospheric parameters for 25 years are shown in Fig. 6 (blue solid line) together with the historical values from the last two solar cycles.

4. Forecast accuracy

To evaluate the forecast accuracy we developed a procedure that compared HelMod modulated spectra for past periods (see,

[8]The procedure can be summarized as follow: if A_i is the normalization factor to be applied to the forecasting template for the cycle i, and A_{i+1} is the normalization factor to be applied to the forecasting template for the cycle $i+1$, then the forecasting template at solar maxima of solar cycle i is normalized using the value A_i. At the next solar minima, the forecasting template is normalized using the value $\frac{A_i+A_{i+1}}{2}$. Finally, at solar maxima of cycle $i+1$ the forecasting template is normalized using the value A_{i+1}.

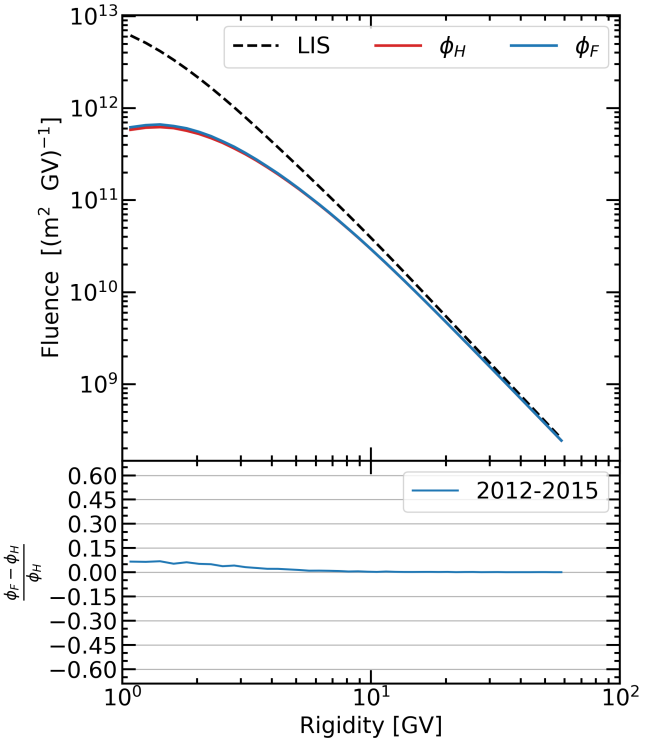

Fig. 7. top panel: Proton differential fluence evaluated with HelMod from Jan 2012 to Jan 2015. Dashed line is the LIS from Boschini et al. (2020b), $\phi_{\rm H}$ is HelMod differential fluence and ϕ_F is the forecast differential fluence. bottom panel: relative difference between HelMod and forecast differential fluences.

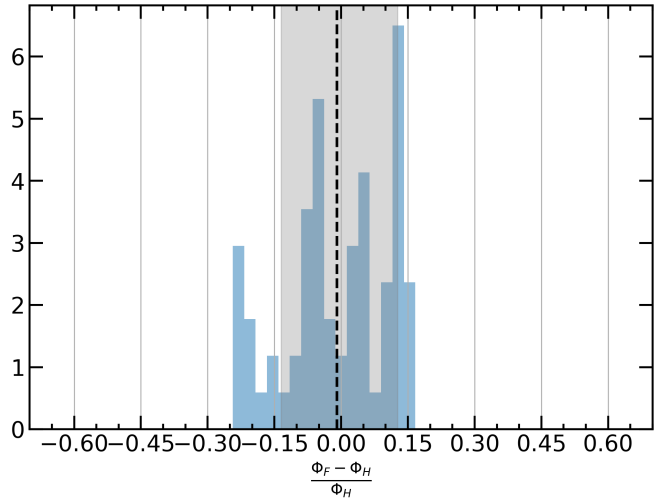

Fig. 8. Distribution of $\frac{\Phi_F - \Phi_{\rm H}}{\Phi_{\rm H}}$, where Φ_F is the forecast fluence integrated over 3 years and $\Phi_{\rm H}$ is HelMod fluence integrated over the same period. *Forecasting parameters* used to evaluate Φ_F are computed as a close-in-time prediction. The dashed line represents the average value while the grey area reports the 68% C.L. range.

e.g., Boschini et al., 2019) with those obtained from the forecasting tool described in Sect. 3.1 and applied back in time before the experimental observation time, i.e., without using the observed heliospheric parameters. As a reference, we consider the period from 2006 to 2017, i.e., the time interval observed by PAMELA (Martucci et al., 2018) and AMS-02 (Aguilar et al., 2018) experiments. In the present analysis, we do not consider the period from the beginning of 2009 to the end of 2010, i.e., at the beginning of solar cycle 24, because of the anomalous long persistence of solar minima conditions (see, e.g., McDonald et al., 2010) that cannot be considered representative for a general case. Since the forecast of GCR is important for assessing the SEE rate over long-duration space missions, we considered the GCR fluence (Φ, expressed in m^{-2}) integrated over several years and on the available rigidity range (i.e. from 0.4 to 47 GV for PAMELA and from 1 to 58 GV for AMS-02). HelMod produces modulated spectral intensities on the base of heliospheric parameters averaged on a Bartel rotation (27 days) period, that represents the reference dataset. For each Bartel rotation, we evaluated the *forecasting parameters* to perform a prediction up to 11 years in the future. Typical simulation outputs are reported in Fig. 7 where the forecasted differential fluence is integrated over 3 years (ϕ_F, expressed in $m^{-2}GV^{-1}$) and are compared with HelMod differential fluence integrated over the same period ($\phi_{\rm H}$). We report in Fig. 8 the distribution of $\frac{\Phi_F - \Phi_{\rm H}}{\Phi_{\rm H}}$ for the considered datasets included in the simulation, where Φ_F is the forecast fluence integrated over 3 years and $\Phi_{\rm H}$ is HelMod fluence integrated over the same period, considering a close-in-time prediction of *forecasting parameters*, i.e., assuming to know the *heliospheric parameters* just before the simulated periods. The dashed line represents the average relative difference while the grey area reports the 68% C.L. range. We repeated this analysis assuming prediction windows from 0 to 11 years. These results are shown in Fig. 9 where we report the average relative difference $< \frac{\Phi_F - \Phi_{\rm H}}{\Phi_{\rm H}} >$ and the corresponding 68% C.L. range for each prediction window. These results indicate that the forecasting procedure can reproduce HelMod fluences with an accuracy below 5% ($\pm$10% at 68% C.L.) for short time predictions (up to 4 years) and below 15% ($\pm(20-25)$% at 68% C.L.) for long time predictions (up to 9 years). Including in the analysis datasets during the anomalous solar minima 2009–2010, the average values obtained are marginally affected and exhibit an increase to $\sim \pm 15$% at the 68% C.L. for 2 years prediction, and to $\sim \pm 40$% at the 68% C.L. for long time predictions. The motivation of this effect is that, after the solar minimum, the solar activity shows a fast rise, thus, a small error in the prediction of the end of the solar cycle leads to a huge discrepancy between actual and forecasted solar activity levels. This analysis was repeated considering various scenarios: we consider forecast fluence integrated over 1–2–3 years, we separately consider AMS-02 and PAMELA periods (i.e., low and high solar activity)and, then, we iterated again again the analysis considering different energy ranges as well as using different *forecasting templates* randomly chosen within the templates uncertainties. All these analyses are compatible with each other and lead to similar conclusions within the limits (< 5% and < 15%) presented in this paper that can be considered as upper limits for accuracy.

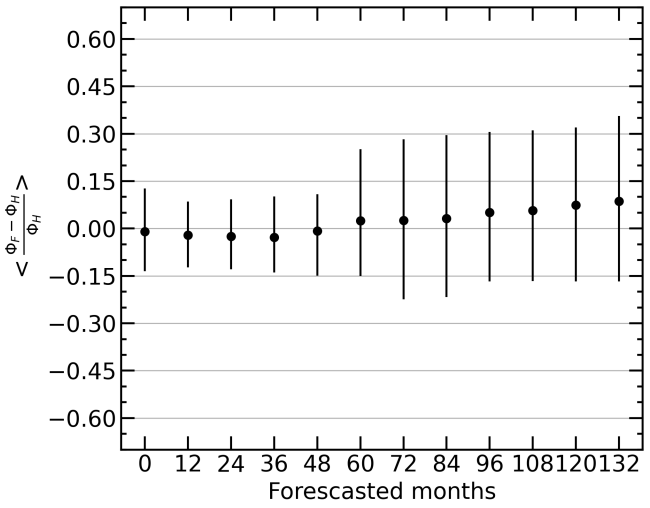

Fig. 9. Average relative difference $< \frac{\Phi_F - \Phi_H}{\Phi_H} >$ along with the corresponding 68% C.L. range evaluated for each prediction windows starting from 0 to 11 years.

5. Conclusions

Solar modulation presents a time periodicity that can be related to *heliospheric parameters*, relevant for cosmic ray propagation in the heliosphere, like SN, IMF, SWS, TAL and SWD. By inspection on how these parameters change with time, time structures common to all the analyzed cycles can be interpolated using a *forecasting template* for a typical solar cycle. The most challenging parameter to be estimated is the length of the solar cycle. A-priori, it is not possible to forecast the length of a solar cycle before it reaches its maximum. Thus, in this case, an average value should be taken, while after the solar maximum is reached, a fitting procedure can return a refined forecast for the end of the current solar cycle. This procedure allows us to forecast *heliospheric parameters* relevant for setting up the HelMod code providing GCR intensity for future space missions. The forecasting procedure was tested by applying it to past periods, where a benchmark can be assessed. We found that, on average, the forecast integrated fluence agrees within ∼ 5–15% better than the actual simulations for 11 years. These results assess the capability of the HelMod model to predict the cosmic rays fluence for future space missions.

Acknowledgements

This work was carried out using the HelMod tool which currently is supported within the framework of space radiation environment activities of ASIF –ASI (Agenzia Spaziale Italiana) Supported Irradiation Facilities–, e.g., ASIF implementation agreements 2017-22-HD.0 ASI-ENEA, 2017-15-HD.0 ASI-INFN, 2021-39-HH.0 ASI-ENEA and ASIF implementation agreement 2021-36-HH.0 involving ASI and Milano-Bicocca University. This work is also supported by ASI contract ASI-INFN No. 2019-19-HH.0 and ESA (European Space Agency) contract 4000116146/16/NL/HK.

Sunspot data were provided by the Marshall Space Flight Center catalogue of Royal Greenwich Observatory and SWPC/NOAA observations. We acknowledge the use of NASA/GSFC's Space Physics Data Facility's OMNIWeb service, and OMNI data.

We wish to specially thank Pavol Bobik, Giuliano Boella, Davide Grandi, Karel Kudela, Simonetta Pensotti, Marian Putis, Davide Rozza, Mauro Tacconi and Mario Zannoni for their support to HelMod code and suggestions.

References

Aguilar, M., Ali Cavasonza, L., Alpat, B. et al. (2018). Observation of Fine Time Structures in the Cosmic Proton and Helium Fluxes with the Alpha Magnetic Spectrometer on the International Space Station. *Physical Review Letters*, *121*(5), 051101. doi:10.1103/PhysRevLett.121.051101.

Aguilar, M., Ali Cavasonza, L., Ambrosi, G., & et al. (2021). The alpha magnetic spectrometer (ams) on the international space station: Part ii – results from the first seven years. *Physics Reports*, *894*, 1 – 116. doi:10.1016/j.physrep.2020.09.003.

Alanko-Huotari, K., Mursula, K., Usoskin, I. G., & Kovaltsov, G. A. (2006). Global Heliospheric Parameters and Cosmic-Ray Modulation: An Empirical Relation for the Last Decades. *Sol. Phys.*, *238*(2), 391–404. doi:10.1007/s11207-006-0233-z.

Baade, W., & Zwicky, F. (1934). Cosmic Rays from Super-novae. *Proceedings of the National Academy of Science*, *20*(5), 259–263. doi:10.1073/pnas.20.5.259.

Bobik, P., Boella, G., Boschini, M. J. et al. (2012). Systematic Investigation of Solar Modulation of Galactic Protons for Solar Cycle 23 Using a Monte Carlo Approach with Particle Drift Effects and Latitudinal Dependence. *Astrophys. J.*, *745*, 132. doi:10.1088/0004-637X/745/2/132.

Bobik, P., Boschini, M. J., Della Torre, S. et al. (2016). On the forward-backward-in-time approach for monte carlo solution of parker's transport equation: One-dimensional case. *Journal of Geophysical Research: Space Physics*, *121*(5), 3920–3930. doi:10.1002/2015JA022237.

Boschini, M. J., Della Torre, S., Gervasi, M., La Vacca, G., & Rancoita, P. (2018a). Propagation of cosmic rays in heliosphere: the helmod model. *Adv. Space Res.*, *62*(10), 2859 – 2879. doi:10.1016/j.asr.2017.04.017.

Boschini, M. J., Della Torre, S., Gervasi, M., La Vacca, G., & Rancoita, P. G. (2019). The helmod model in the works for inner and outer heliosphere: From ams to voyager probes observations. *Adv. Space Res.*, *64*(12), 2459 – 2476. doi:10.1016/j.asr.2019.04.007.

Boschini, M. J., Della Torre, S., Gervasi, M. et al. (2017a). The helmod monte carlo model for the propagation of cosmic rays in heliosphere. *Proceedings of the International Astronomical Union, Proceedings of IAU Symposium 335 - Space Weather of the Heliosphere: Processes and Forecasts, July 17-21, 2017, University of Exeter, UK*, *13*(S335), 276–279. doi:10.1017/S1743921317007359. arXiv:1708.04690.

Boschini, M. J., Della Torre, S., Gervasi, M. et al. (2017b). Solution of Heliospheric Propagation: Unveiling the Local Interstellar Spectra of Cosmic-ray Species. *Astrophys. J.*, *840*, 115. doi:10.3847/1538-4357/aa6e4f.

Boschini, M. J., Della Torre, S., Gervasi, M. et al. (2018b). Deciphering the local interstellar spectra of primary cosmic-ray species with helmod. *Astrophys. J.*, *858*(1), 61. doi:10.3847/1538-4357/aabc54.

Boschini, M. J., Della Torre, S., Gervasi, M. et al. (2018c). Helmod in the works: From direct observations to the local interstellar spectrum of cosmic-ray electrons. *Astrophys. J.*, *854*(2), 94. doi:10.3847/1538-4357/aaa75e.

Boschini, M. J., Della Torre, S., Gervasi, M. et al. (2020a). Deciphering the local interstellar spectra of secondary nuclei with the galprop/helmod framework and a hint for primary lithium in cosmic rays. *Astrophys. J.*, *889*(2), 167. doi:10.3847/1538-4357/ab64f1.

Boschini, M. J., Della Torre, S., Gervasi, M. et al. (2020b). Inference of the local interstellar spectra of cosmic-ray nuclei z < 28 with the GalProp-HelMod framework. *Astrophys. J. Supplement*, *250*(2), 27. doi:10.3847/1538-4365/aba901.

Boschini, M. J., Della Torre, S., Gervasi, M. et al. (2021a). A Hint of a Low-Energy Excess in Cosmic-Ray Fluorine. *submitted to Astrophys. J., arxiv:2106.01626*, .

Boschini, M. J., Della Torre, S., Gervasi, M. et al. (2021b). The discovery of a low-energy excess in cosmic-ray iron: Evidence of the past supernova activity in the local bubble. *The Astrophysical Journal*, *913*(1), 5. doi:10.3847/1538-4357/abf11c.

Cliver, E. W., & Ling, A. G. (2001). 22 Year Patterns in the Relationship of Sunspot Number and Tilt Angle to Cosmic-Ray Intensity. *Astrophys. J. Letter*, *551*(2), L189–L192. doi:10.1086/320022.

Cummings, A. C., Stone, E. C., Heikkila, B. C. et al. (2016). Galactinc cosmic rays in the local interstellar medium: Voyager 1 observations and model results. *The Astrophysical Journal*, *831*(1), 18. doi:10.3847/0004-637x/831/1/18.

Della Torre, S., Bobik, P., Boschini, M. J. et al. (2012). Effects of solar modulation on the cosmic ray positron fraction. *Adv. Space Res.*, *49*, 1587–1592. doi:10.1016/j.asr.2012.02.017.

Durante, M., & Cucinotta, F. A. (2008). Heavy ion carcinogenesis and human space exploration. *Nature Reviews Cancer*, *8*(6), 465–472. doi:10.1038/nrc2391.

ECSS (2008). *ECSS-E-ST-10-04C Space engineering - Space Environment*. ESA-ESTEC Requirements and Standards Division, Noordwijk, The Netherlands.

Fiandrini, E., Tomassetti, N., Bertucci, B. et al. (2021). Numerical modeling of cosmic rays in the heliosphere: Analysis of proton data from ams-02 and pamela. *Phys. Rev. D*, *104*, 023012. doi:10.1103/PhysRevD.104.023012.

Fisk, L. (1971). Solar modulation of galactic cosmic rays. *J. Geophys. Res.-Space*, *76*(1), 221–226. doi:10.1029/JA076i001p00221.

Gleeson, L. J., & Axford, W. I. (1967). Cosmic rays in the interplanetary medium. *Astrophys. J.*, *149*, L115–L118. doi:10.1086/180070.

Gonzalez-Velo, Y., Barnaby, H. J., & Kozicki, M. N. (2017). Review of radiation effects on ReRAM devices and technology. *Semiconductor Science Technology*, *32*(8), 083002. doi:10.1088/1361-6641/aa6124.

Hathaway, D. H. (2015). The Solar Cycle. *Living Reviews in Solar Physics*, *12*, 4. doi:10.1007/lrsp-2015-4.

Heber, B., Potgieter, M. S., & Ferrando, P. (1997). Solar modulation of galactic cosmic rays: the 3D heliosphere. *Adv. Space Res.*, *19*, 795–804. doi:10.1016/S0273-1177(96)00149-4.

Hoeksema, J. T. (1995). The Large-Scale Structure of the Heliospheric Current Sheet During the ULYSSES Epoch. *Space Sci. Rev.*, *72*, 137–148. doi:10.1007/BF00768770.

Jokipii, J. R. (1971). Propagation of cosmic rays in the solar wind. *Rev. Geoph. Space Phys.*, *9*, 27–87. doi:10.1029/RG009i001p00027.

Jokipii, J. R., Levy, E. H., & Hubbard, W. B. (1977). Effects of particle drift on cosmic-ray transport. I - General properties, application to solar modulation. *Astrophys. J.*, *213*, 861–868. doi:10.1086/155218.

Jokipii, J. R., & Parker, E. N. (1970). on the Convection, Diffusion, and Adiabatic Deceleration of Cosmic Rays in the Solar Wind. *Astroph. J.*, *160*, 735–744. doi:10.1086/150465.

King, J. H., & Papitashvili, N. E. (2005). Solar wind spatial scales in and comparisons of hourly Wind and ACE plasma and magnetic field data. *J. Geophys. Res.-Space*, *110*(A9), A02104. doi:10.1029/2004JA010649.

Koyama, K., Petre, R., Gotthelf, E. V., Hwang, U., Matsuura, M., Ozaki, M., & Holt, S. S. (1995). Evidence for shock acceleration of high-energy electrons in the supernova remnant SN1006. *Nature*, *378*(6554), 255–258. doi:10.1038/378255a0.

Martucci, M., Munini, M., Boezio, M. et al. (2018). Proton Fluxes Measured by the PAMELA Experiment from the Minimum to the Maximum Solar Activity for Solar Cycle 24. *Astrophys. J.*, *854*(1), L2. doi:10.3847/2041-8213/aaa9b2.

McDonald, F. B., Webber, W. R., & Reames, D. V. (2010). Unusual time histories of galactic and anomalous cosmic rays at 1 au over the deep solar minimum of cycle 23/24. *Geophysical Research Letters*, *37*(18), L18101. doi:https://doi.org/10.1029/2010GL044218.

Nandy, D. (2021). Progress in Solar Cycle Predictions: Sunspot Cycles 24-25 in Perspective. *Sol. Phys.*, *296*(3), 54. doi:10.1007/s11207-021-01797-2.

Owens, M. J., Lockwood, M., Barnard, L., & Davis, C. J. (2011). Solar cycle 24: Implications for energetic particles and long-term space climate change. *Geoph. Res. Lett.*, *38*(19), L19106. doi:10.1029/2011GL049328.

Parker, E. N. (1965). The passage of energetic charged particles through interplanetary space. *Plan. Space Sci.*, *13*, 9–49. doi:10.1016/0032-0633(65)90131-5.

Potgieter, M. S. (2013). Solar Modulation of Cosmic Rays. *Living Reviews in Solar Physics*, *10*, 3. doi:10.12942/lrsp-2013-3.

Samwel, S. W., El-Aziz, E. A., Garrett, H. B., Hady, A. A., Ibrahim, M., & Amin, M. Y. (2019). Space radiation impact on smallsats during maximum and minimum solar activity. *Adv. Space Res.*, *64*(1), 239–251. doi:10.1016/j.asr.2019.03.025.

Samwel, S. W., & Hady, A. A. (2009). Space radiation environment forecast for egyptsat-2 satellite. *Space Weather*, *7*(12), S12004. doi:10.1029/2009SW000482.

Simpson, J. A. (1996). Ulysses cosmic-ray investigations extending from the south to the north polar regions of the Sun and heliosphere. *Nuovo Cimento C Geophysics Space Physics C*, *19*, 935–943. doi:10.1007/BF02508134.

Simpson, J. A., Anglin, J. D., Balogh, A. et al. (1992). The ULYSSES Cosmic Ray and Solar Particle Investigation. *Astronomy and Astrophysics Supplement Series*, *92*, 365–399.

Stone, E. C., Cummings, A. C., Heikkila, B. C., & Lal, N. (2019). Cosmic ray measurements from Voyager 2 as it crossed into interstellar space. *Nature Astronomy*, *3*, 1013–1018. doi:10.1038/s41550-019-0928-3.

Stone, E. C., Cummings, A. C., McDonald, F. B. et al. (2005). Voyager 1 Explores the Termination Shock Region and the Heliosheath Beyond. *Science*, *309*, 2017–2020. doi:10.1126/science.1117684.

Stone, E. C., Cummings, A. C., McDonald, F. B. et al. (2013). Voyager 1 Observes Low-Energy Galactic Cosmic Rays in a Region Depleted of Heliospheric Ions. *Science*, *341*, 150–153. doi:10.1126/science.1236408.

Usoskin, I. G. (2017). A history of solar activity over millennia. *Living Reviews in Solar Physics*, *14*(1), 3. doi:10.1007/s41116-017-0006-9.

Webber, W. R., & McDonald, F. B. (2013). Recent Voyager 1 data indicate that on 25 August 2012 at a distance of 121.7 AU from the Sun, sudden and unprecedented intensity changes were observed in anomalous and galactic cosmic rays. *Geoph. Res. Lett.*, *40*, 1665–1668. doi:10.1002/grl.50383.